

# Nuclear gas dynamics in Arp 220 – sub-kiloparsec scale atomic hydrogen disks

C.G. Mundell<sup>1,2,3</sup>

cgm@astro.umd.edu

P. Ferruit<sup>2,4</sup>

ferruit@cumulus.univ-lyon1.fr

A. Pedlar<sup>5</sup>

ap@jb.man.ac.uk

## ABSTRACT

We present new, high angular resolution ( $\sim 0''.22$ ) MERLIN observations of neutral hydrogen (H I) absorption and  $\lambda 21$ -cm radio continuum emission across the central  $\sim 900$  parsecs of the ultraluminous infrared galaxy, Arp220. Spatially resolved H I absorption is detected against the morphologically complex and extended  $\lambda 21$ -cm radio continuum emission, consistent with two counterrotating disks of neutral hydrogen, with a small bridge of gas connecting the two. Column densities across the two nuclei are high, lying in the range  $8 \times 10^{19} T_s(K) \lesssim N_H \lesssim 2.4 \times 10^{20} T_s(K) \text{ cm}^{-2}$  ( $T_s$  is spin temperature) and corresponding to optical extinctions of  $0.052 T_s(K) \lesssim A_V \lesssim 0.155 T_s(K) \text{ mag}$ , with the higher column densities in the eastern nucleus. Velocity gradients are clearly visible across each nucleus, reaching  $1010 \pm 20 \text{ km s}^{-1} \text{ kpc}^{-1}$  in  $\text{PA} \sim 55^\circ$  and  $830 \pm 20 \text{ km s}^{-1} \text{ kpc}^{-1}$  in  $\text{PA} \sim 270^\circ$  for eastern and western nuclei respectively. These gradients imply dynamical masses  $M_D = 1.1 \times 10^9 (\sin^{-2} i) M_\odot$  (E) and

---

<sup>1</sup>Astrophysics Research Institute, Liverpool John Moores University, Twelve Quays House, Egerton Wharf, Birkenhead, CH41 1ID, UK

<sup>2</sup>Department of Astronomy, University of Maryland, College Park, MD20742, USA

<sup>3</sup>Royal Society University Research Fellow

<sup>4</sup>Centre de Recherche Astronomique de Lyon, 9 av. Charles André, 69561 Saint-Genis Laval Cedex, France

<sup>5</sup>University of Manchester, Jodrell Bank Observatory, Macclesfield, Cheshire, SK11 9DL, UK

$1.7 \times 10^8 (\sin^{-2}i) M_\odot$  (W), assuming the neutral gas is distributed in two thin circularly rotating disks.

We propose a merger model in which the two nuclei represent the galaxy cores which have survived the initial encounter and are now in the final stages of merging, similar to conclusions drawn from previous CO studies (Sakamoto, Scoville & Yun 1999 - SSY99 hereafter). However, we suggest that instead of being coplanar with the main CO disk (in which the eastern nucleus is embedded), the western nucleus lies above it and, as suggested by bridge of H I connecting the two nuclei, will soon complete its final merger with the main disk. We suggest that the collection of radio supernovae (RSN) detected in VLBA studies in the more compact western nucleus represent the second burst of star formation associated with this final merger stage and that free-free absorption due to ionised gas in the bulge-like component can account for the observed RSN distribution.

*Subject headings:* galaxies: individual (Arp 220); galaxies: kinematics and dynamics; galaxies: nuclei

## 1. Introduction

Ultra-Luminous Infra-Red Galaxies (ULIRGs), identified by IRAS and defined by their high far-infrared luminosities ( $>10^{12} L_\odot$ ), have spectral energy distributions dominated by the 8-1000- $\mu\text{m}$  mid-far IR emission (e.g., Soifer et al. 1987; Clements et al. 1996a; Sanders & Mirabel 1996) and show luminosities and space densities in the local Universe similar to those of QSOs (Soifer 1986; Soifer, Houck & Neugebauer 1987). The excess of far-IR emission in these objects is generally thought to indicate the presence of large amounts of hot dust, but the mechanism for heating the dust remains controversial. Intense nuclear starbursts and heavily-shrouded active galactic nuclei (AGN) have both been advocated and a combination of both energy sources currently seems likely, with starbursts dominating at  $L_{\text{IR}} < 10^{12.3} L_\odot$  and the AGN-dominated fraction increasing to 35%–50% above this luminosity (Genzel et al. 1998; Veilleux, Sanders & Kim 1999).

ULIRGs are almost always found in strongly interacting systems or advanced mergers (Clements et al. 1996a,b; Clements & Baker 1996), during which large-scale torques on the intersteller medium and loss of angular momentum drives gas towards the central few kilo-parsecs of the system, where it is thought to result in intense starburst and/or AGN activity (e.g., Barnes & Hernquist 1991; Mihos & Hernquist 1994, 1996; Norman & Scoville 1988). In this scenario, an (obscured) AGN is switched on as the galaxy merger reaches an advanced state, and is then progressively unveiled as the circumnuclear starburst processes

(and expels) the surrounding gas. Obscuration is high in the mid-IR emitting regions of ULIRGs, with model-dependent extinctions ranging from  $A_V \sim 5 - 1000$  (Genzel et al. 1998). However, progression from starburst- to AGN-powered emission as the merger advances is not evident in present studies (e.g., Genzel et al. 1998). If ULIRGs do contain obscured progenitors of future optically-bright quasars (e.g. Sanders et al. 1988) they may offer a valuable opportunity to study an important stage in the evolution of quasars (and powerful radio galaxies) in the local Universe. Alternatively, highly obscured AGN might not be common in the ULIRG population since strong AGN activity, once triggered, might quickly destroy the obscuring screen, producing an easily detectable AGN (e.g. Lutz, Veilleux & Genzel 1999).

In this context, the prototypical ULIRG Arp 220 (IC4553/4, UGC09913), a double-nucleus system, is an extremely interesting object. In the diagnostic diagrams of Genzel et al. (1998, their Fig. 5) it appears as one of the most completely starburst-powered ULIRG in their sample, despite the fact that it is in an advanced merger state. In these final stages of merging, peak gas densities (and related activity) are thought to occur, when the merging galaxies are within a  $\sim$ kpc of one another and are in the process of coalescing (Mihos & Hernquist 1996); high angular resolution observations of the central kiloparsec are therefore vital to determine the gas dynamics in this important region. This paper presents the first subarcsecond-resolution, spatially-resolved spectral imaging of the distribution and kinematics of neutral hydrogen ( $\text{H}\text{I}$ ) in the central 900 pc of Arp 200, improving on previous observations by more than a factor of ten in angular resolution.

$\text{H}\text{I}$  is a valuable tracer of galactic structure and dynamics over a wide range of size scales and is a valuable tool for probing the gaseous conditions in the highly-obscured, compact nuclear regions of ULIRGs which are often unaccessible at optical wavelengths. Indeed ULIRGs contain large amounts of neutral hydrogen (e.g.  $N_{\text{H}} > 10^{21} - 10^{22}$  atoms  $\text{cm}^{-2}$  - Mirabel 1982), and recent VLA synthesis maps of  $\text{H}\text{I}$  *emission* in objects such as Arp 220 (Hibbard, Vacca, & Yun 2000), have revealed massive gaseous tidal features ( $M_{\text{H}} > 10^9 M_{\odot}$ ) extending over several tens of kpc beyond the optical emission and demonstrating the dramatic redistribution of material during galaxy merger. Unfortunately, such studies of  $\text{H}\text{I}$  in *emission* are limited by surface brightness sensitivity to angular resolutions of  $> 6'' - 10''$  with current instruments. Instead,  $\text{H}\text{I}$  *absorption* measurements can be performed to angular resolutions as high as a few milliarcseconds in the presence of a bright radio continuum background source (e.g. Peck & Taylor 1998; Carilli & Taylor 2000); subarcsecond resolutions achievable with MERLIN probe the distribution and kinematics of  $\text{H}\text{I}$ , in absorption, on scales of  $\sim 10 - 100$  pc in nearby galaxies (e.g. Mundell et al. 1995; Cole et al. 1998).

Here we present new,  $0''.22$  (81-pc) resolution,  $\lambda 21\text{-cm}$   $\text{H}\text{I}$  absorption observations of the

central  $\sim$ 900 pc of Arp 220 with MERLIN. The observations and data analysis are described in Sect. 2 and the results in Sect. 3. We then compare the derived masses with those obtained from the molecular gas observations, and discuss the present geometry of the system and the history of the merger in view of these new observations and the available data. We adopt a distance of  $\sim 77$  Mpc for Arp 220, at which  $1''$  correspond to  $\sim 370$  pc.

## 2. Observations and Data Analysis

### 2.1. Observations and data calibration

The central region of Arp 220 was observed at  $\lambda$ 21 cm, on 26th January, 1996, with the Multi-Element Radio Linked Interferometer (MERLIN), which at this time consisted of 8 telescopes (including the 76-m Lovell telescope). The maximum baseline length of the array is 217 km, corresponding to  $\sim 1$  M $\lambda$  at  $\lambda$ 21 cm and yielding an effective spatial resolution of  $0''.22$ . Dual polarizations were recorded for an 8-MHz bandwidth in spectral line mode, with 64 channels per polarization, resulting in a channel width of 125 kHz (26.3 km s $^{-1}$ ). As the first channel is reserved for on-line information, the centre of the band lies at channel 31.5, corresponding to an optical heliocentric velocity of 5496.2 km s $^{-1}$ . Total observing time on Arp 220 was  $\sim$ 7 hours, with 2 minutes observations of the phase calibrator 1551+239 interleaved every 5 minutes throughout the observations. Absolute flux calibration was determined from observations of 3C286, assuming a flux density of 14.731 Jy at 1420.4 MHz (Baars et al. 1977). 0552+398 was used to determine bandpass corrections for the spectral line data.

After preliminary amplitude calibration and gain-elevation corrections were applied, using local MERLIN software, the data were transferred to the NRAO Astronomical Image Processing System (AIPS - van Moorsel, Kemball & Greisen 1996) for all subsequent calibration, editing and imaging. Standard calibration and data editing (Greisen & Murphy 1998) were performed on the ‘pseudo-continuum’ dataset, which is formed by averaging the central 75% (6 MHz) of the band (analogous to the VLA ‘channel 0’ dataset). The resulting map of the phase calibrator was used to guide additional data editing and self-calibration; the derived phase and gain corrections were applied to the Arp 220 pseudo-continuum data, from which a preliminary image was produced and used in further data editing and phase self-calibration. The total corrections and data flags were then applied to the spectral line data and bandpass calibration was performed. Due to good bandpass stability, no significant improvement to the continuum images was achieved by iteratively performing self-calibration and bandpass calibrations. Finally, the telescopes were reweighted according to their gains.

The continuum contribution (formed from the line-free channels 5-15 and 50-60) was subtracted in the  $(u, v)$  plane using AIPS task UVLIN. The corresponding ‘true’ continuum dataset was formed from the same line-free channels in the  $(u, v)$  plane using AVSPC. These two datasets were then Fourier transformed with uniform weighting (pixel size 45 mas), deconvolved and added together to form the absorption cube ( $512 \times 512 \times 63$ ) with the correct continuum level adjacent to the line. A circular restoring beam of size  $0''.22$  was used for both datasets and the r.m.s. noise levels were  $\sim 0.1$  mJy beam $^{-1}$  and  $0.5$  mJy beam $^{-1}$  per channel for the continuum image and spectral line cube, respectively.

### 2.1.1. Positional Accuracies

The commonly-used phase-referencing technique of interspersing observations of the target source with regular and frequent observations of a nearby calibrator with known position allows the absolute position of the target source to be determined; the accuracy of the calibrator position is therefore important. Our phase calibrator, 1551+239, was originally identified in the calibrator survey of Patnaik et al. (Patnaik et al. 1992; Browne et al. 1998) and lies in ‘Region 2’ or declination range  $20\text{--}35^\circ$  (Wilkinson et al. 1998). The typical positional uncertainty for the survey is 50 mas but ‘Region 2’ suffered from larger systematic errors than other regions of the survey. The origin of these errors is unknown and the positional uncertainty for 1551+239, which was omitted from the final published survey, might be as large as 100 mas, predominantly in declination (Thomasson, private communication). Positions derived from previous VLA images at 5 GHz (Baan & Haschick (1995), 15 and 22 GHz (Norris, 1988) also show a range of values, differing primarily in declination by  $\sim 100\text{--}200$  mas. Consequently, the positional uncertainty for Arp 220 is no better than 100 mas.

Nevertheless, the derived position for the western nucleus,  $\alpha_{\text{B1950}} = 15^h32^m46\rlap{.}^s89142\rlap{.}^s$ ,  $\delta_{\text{B1950}} = 23^\circ40'08\rlap{.}''0215$ , compares well with positions derived from CO observations by SSY99,  $\alpha_{1950} = 15^h32^m46\rlap{.}^s88\rlap{.}^s$ ,  $\delta_{1950} = 23^\circ40'08\rlap{.}''0$  ( $\pm 0\rlap{.}''1$ ), and 5-GHZ MERLIN observations by Baan (private communication),  $\alpha_{1950} = 15^h32^m46\rlap{.}^s89053\rlap{.}^s$ ,  $\delta_{1950} = 23^\circ40'08\rlap{.}''0509$ . It should be noted that although the positional uncertainties limit very accurate absolute registration with observations from other instruments, the MERLIN results presented here are not otherwise affected since Arp 220 is strong enough for self-calibration to be performed.

## 2.2. Analysis of the H I absorption profiles

Examination of the observed H I absorption line profiles revealed that not all are well approximated by a single Gaussian profile, due to the presence of additional narrow components and/or wings overimposed on the main, relatively broad component. Simple, automatic moment analysis is therefore difficult and may result in corrupted velocity fields, where a single Gaussian component does not represent the centroid velocity accurately. We therefore performed a multiple Gaussian profile fitting of the absorption spectra using a modified version of the FIT/SPEC software (Rousset 1992), originally developed to fit optical emission lines.

The fitting was performed in two stages. First a single Gaussian profile was fitted automatically to each absorption spectrum and residuals were examined to detect regions where additional components were likely to be present (i.e. regions with residuals higher than three times the  $\sigma = 0.5$  mJy beam $^{-1}$  noise level) - these regions coincided with each nucleus. For each nucleus, the spectral characteristics of the additional components were then determined by fitting to individual spectra with the most contrast. Next, a multi-component Gaussian fit to the line profiles was performed, using one relatively broad Gaussian component (the ‘main’ component) and a set of narrower components with fixed characteristics (see Table 1). This second step was successful for the western nucleus which exhibited the strongest, most distinct, additional components, but failed for the eastern nucleus where the additional components were poorly contrasted (peak amplitude typically lower than  $6\sigma$ ). Therefore, the moment maps presented in this paper correspond to a single Gaussian component fit to spectra from off-nuclear regions and the eastern nucleus, and a multiple Gaussian component fit to spectra from the western nucleus. Errors on the centroid velocity in the eastern nucleus due to the use of a single Gaussian profile are typically lower than 10 km s $^{-1}$ .

## 3. Results

### 3.1. $\lambda$ 21-cm radio continuum emission

The MERLIN image of the  $\lambda$ 21-cm (1.4-GHz) radio continuum emission from the nuclear region of Arp 220 is shown in Figure 1. The two nuclei (Baan et al. 1987; Norris 1988; Baan & Haschick 1995, BH95 hereafter) are clearly resolved and are embedded in more complex extended emission. The nuclei are labelled E and W in Figure 1 (labelled A and B in the 5-GHz image of BH95). Their peak and integrated fluxes<sup>6</sup> are  $28.7 \pm 1.4$  mJy beam $^{-1}$  &

---

<sup>6</sup>The uncertainty in the flux scale is taken to be 5% and is included in the total uncertainties in flux densities; these errors were derived by adding, in quadrature, the 5% amplitude error, the rms noise in the

$126.5 \pm 6.4$  mJy (E) and  $64.9 \pm 3.3$  mJy beam $^{-1}$  &  $129.3 \pm 6.5$  mJy (W), respectively. The total integrated flux density of the source is  $\sim 285.4 \pm 14.3$  mJy. A large-area box flux yields a slightly higher integrated flux, indicating the presence of structures extended on scales larger than  $1''$ - $2''$ . The presence of extended emission is also suggested by the higher integrated flux densities of 302 mJy (White & Becker, 1992) and 312 mJy (Condon & Dressel, 1978) measured with single dish telescopes at 1.4 GHz and 2.4 GHz respectively. Gaussian fitting to the MERLIN image reveals that the eastern nucleus is well resolved (as can be seen in Figure 1), with a deconvolved size (FWHM) of  $440 \times 345$  mas (i.e.  $\sim 160 \times 130$  pc) in  $PA = 55.0 \pm 0.7$ . The western nucleus is only marginally resolved with a deconvolved size (FWHM) of  $245 \times 190$  mas (i.e.  $90 \times 70$  pc) in  $PA = 96.3^\circ \pm 0.7$ . The derived position for the western nucleus is  $\alpha_{1950} = 15^h 32^m 46.89142s$ ,  $\delta_{1950} = 23^\circ 40' 08.0215$  which corresponds well with observations at other frequencies (see Section 2.1.1 for full discussion).

In addition to emission from the two nuclei, a tongue of  $\lambda$ 21-cm continuum emission is seen to the south-east of the western nucleus (Figure 1) and corresponds to emission previously identified by BH95 (component C in their paper) at 5 GHz. Similar weak extensions are seen around the eastern nucleus. Finally, a broad spur of continuum emission (labelled T in Figure 1) is seen north-west of the western nucleus. It extends over  $0''.8$  in  $PA \sim -50^\circ$ . This weak component is detected over  $\sim 11$  beam areas, with a peak flux density of  $\sim 1.6$  mJy beam $^{-1}$  and an integrated flux density of 6.6 mJy beam $^{-1}$ . There is a hint for the presence of a similar component in the 5-GHz naturally weighted image of BH95 (their Fig. 1, upper panel), but their angular resolution ( $0''.43$ ) is insufficient to deblend it from the emission of the western nucleus.

### 3.2. Neutral Hydrogen Absorption

Figure 2 shows the MERLIN spectral channel images of H I absorption detected across the central  $\sim 600$  pc of Arp 220. Comparison of the channel images with the continuum image, which is displayed to the same scale in the top left panel, shows that absorption is clearly detected against each continuum nucleus, as well as against the bridge of continuum that connects the two nuclei. Figure 3 shows some representative absorption spectra, taken from eight locations across the continuum structure; many of the absorption lines are asymmetric with some showing additional velocity components (e.g. location ‘ER’).

The ability to image neutral gas in absorption depends on both the structure of the background continuum emission and the distribution of the foreground absorbing gas; the

---

image and the error in the Gaussian fitting.

neutral gas in Arp 220 is spatially extended and so the absorption is well resolved at this angular resolution, in particular against the extended continuum emission of the eastern nucleus. The velocity range over which absorption is detected ranges from  $\sim 5160 \text{ km s}^{-1}$  to  $5725 \text{ km s}^{-1}$  and compares well with the width of the single dish absorption line at 10% of the peak absorption (Mirabel & Sanders 1988). However, this is lower than the full width at zero intensity (FWZI) of the single dish profile,  $\sim 640 \text{ km s}^{-1}$  (Mirabel & Sanders 1988). If weak absorption is present against weak, extended radio continuum emission, this absorption would not be detectable in the MERLIN observations, and this may explain the additional 50- $\text{km s}^{-1}$  width at the red and blue extremes of the single dish profile.

HI absorption is not detected against the continuum component C, to the south-east of the western nucleus (Figure 3), to a limiting  $3\sigma$  absorption depth of  $1.5 \text{ mJy beam}^{-1}$ . Assuming a constant column density across C, this implies a maximum column density  $N_{\text{H}} \sim 1.7 \times 10^{19} T_{\text{s}}(\text{K}) \text{ cm}^{-2}$ , where  $T_{\text{s}}(\text{K})$  is the spin temperature for which the exact value is unknown but is found to be typically  $\sim 10^2$ – $10^4 \text{ K}$  in the Galaxy (Heiles & Kulkarni 1988). The weakness of continuum component C prevents the determination of stringent upper limits for  $N_{\text{H}}$ , but the relatively blue colour of the infrared component coincident with C (Scoville et al. 1998) provides support for a low column density in this region.

Very weak HI absorption may be present against the spur of weak, extended continuum emission (T) to the north-west of the western nucleus, but the continuum emission is weak in this region (peak flux density  $\sim 1.6 \text{ mJy beam}^{-1}$ ), preventing a reliable determination of column density; a  $3\sigma$  detection would require a column density  $N_{\text{H}} > 1.3 \times 10^{20} T_{\text{s}}(\text{K}) \text{ cm}^{-2}$ . Close inspection of the spectral channel images in Figure 2, over a velocity range  $\sim 5500$ – $5300 \text{ km s}^{-1}$ , suggests a possible weak absorption component extended in the same PA as the continuum extension ( $\sim -50^\circ$ ), but more sensitive observations would be required to confirm its detection and measure the column density.

Figure 4 shows the two-dimensional column density distribution and velocity field of the main kinematic component, as derived from multi-component Gaussian profile fitting of the spectra (see Sect. 2.2). Characteristics of the main and additional kinematic components in the eight spectra displayed in Figure 3 are listed in Table 1 and examples of Gaussian fitting to components in the eastern and western disks are shown in Figure 5 and Figure 6, respectively. The two nuclei are spatially well separated at this resolution (as shown in Figure 2) and a velocity gradient is clearly visible across each nucleus. Across the eastern nucleus, the velocity gradient is  $1010 \pm 20 \text{ km s}^{-1} \text{ kpc}^{-1}$  in PA  $\sim 55^\circ$ , while the marginally resolved western nucleus shows a gradient of  $830 \pm 20 \text{ km s}^{-1} \text{ kpc}^{-1}$  in PA  $\sim 270^\circ$ .

### 3.2.1. Nuclear Column Densities

The neutral hydrogen column densities across the two nuclei are high, lying in the range  $8 \times 10^{19} \text{ T}_s(\text{K}) \lesssim N_{\text{H}} \lesssim 2.4 \times 10^{20} \text{ T}_s(\text{K}) \text{ cm}^{-2}$ , with the higher column densities generally being found in the eastern nucleus. The corresponding optical extinctions, if  $\text{H}\text{I}$  column density and optical extinction in Arp 220 follow the same relation as that seen in the Galaxy (Staveley-Smith & Davies 1987), are  $0.052 \text{ T}_s(\text{K}) \lesssim A_V \lesssim 0.155 \text{ T}_s(\text{K}) \text{ mag}$  and are detailed in Tab. 1. The  $\text{H}\text{I}$  spin temperature is unknown, but for the minimum  $\text{H}\text{I}$  spin temperature  $T_s \sim 100\text{--}200 \text{ K}$ , these extinction values compare well with those derived by Scoville et al. (1998) from high resolution infrared *HST* NICMOS images at 1.1, 1.6 and  $2.22 \mu\text{m}$  and confirm that the radio continuum nuclei lie in regions of relatively high extinction.

An estimate of the column density of molecular hydrogen can be inferred from the CO observations of SSY99, who measured integrated CO fluxes  $S_{\text{CO}(2-1)} = 120 \text{ Jy km s}^{-1}$  (E) and  $187 \text{ Jy km s}^{-1}$  (W). Assuming an excitation temperature of  $40 \text{ K}$ , a CO:H<sub>2</sub> abundance  $X(\text{CO}) = 2.7 \times 10^{-4}$  (Lacy et al. 1994) and optically thin emission, we infer H<sub>2</sub> column densities  $N_{\text{H}_2} \sim 2.8 \times 10^{22} \text{ cm}^{-2}$  (E) and  $4.3 \times 10^{22} \text{ cm}^{-2}$  (W). These values are comparable to the mean  $\text{H}\text{I}$  column densities  $N_{\text{H}} = 1.6 \times 10^{20} \text{ T}_s \text{ cm}^{-2}$  (E) and  $1.3 \times 10^{20} \text{ T}_s \text{ cm}^{-2}$  (W) for  $T_s \sim 100\text{--}200 \text{ K}$  and result in total hydrogen column densities  $N(\text{H}) \sim 4.4 \times 10^{22} \text{ cm}^{-2}$  (E) and  $5.6 \times 10^{22} \text{ cm}^{-2}$  (W); these column densities are likely to be lower limits due to the uncertainty in the values of  $T_s$  (Heiles & Kulkarni 1988) and  $X(\text{CO})$  (Frerking, Langer & Wilson 1982), excitation conditions and optical depth.

Indeed, the nature of the IR emission in Arp 220, AGN or starburst-driven, has long been controversial and the amount of obscuration present is important. High frequency observations have failed to find a hard X-ray or soft  $\gamma$ -ray component consistent with an AGN, suggesting that the column density required to obscure any hidden AGN must be  $N_{\text{H}} \gtrsim 10^{25} \text{ cm}^{-2}$  (Rieke 1988; Dermer et al. 1997). Alternatively, if  $N_{\text{H}} \lesssim 10^{24} \text{ cm}^{-2}$ , more than 80% of the total IR luminosity must have a non-AGN origin. Even if the  $\text{H}\text{I}$  spin temperature is as high as  $T_s \sim 10^4 \text{ K}$ , as might be expected in the vicinity of strong radio continuum emission, the peak measured column density is  $N_{\text{H}} \sim 2.4 \times 10^{24} \text{ cm}^{-2}$ , suggesting that either a large additional quantity of ionized and molecular gas is required to provide the necessary obscuration towards any AGN component or the IR emission is dominated by a starburst.

## 4. Discussion

### 4.1. The nuclear disks

The kinematics of the main absorption component are consistent with two counterrotating disks associated with the two nuclei. We therefore confirm the results from the lower spatial resolution (0''.5) CO observations of Sakamoto et al. (1999). In particular, the velocity field of the disk in the more compact western nucleus is clearly apparent in our higher resolution (0''.22) observations. The kinematic major axis for this western nuclear disk ( $\sim 270^\circ$ ) is consistent with the value inferred from the CO observations ( $263^\circ$ , SSY99, their Tab. 1) but is perpendicular to the north-south velocity gradient inferred from the formaldehyde emission observations of BH95.

This discrepancy can be explained if the gaseous component responsible of the formaldehyde emission is distinct from the western disk gas. The location of the peak of formaldehyde emission,  $\sim 0''.1$  south of the western radio continuum peak (BH95), is coincident with the position of the group of luminous radio supernovae detected by Smith et al. (1998). This suggests that the source of the pumping photons is the intense starburst occurring in the western disk and therefore belongs to it. However, the masing gas can be located far away from the continuum source. Baan, Güsten & Haschick (1986) give *upper limits* on the distance between the continuum source and the masing gas in Arp 220 ranging from 250 pc to 1.1 kpc. Given these upper limits, the masing gas could be molecular gas located in front of the western nucleus and unrelated to the western nuclear disk or a warp in the eastern/large-scale molecular disk. Indeed, the horizontal isovelocity contours of CO(2-1) emission seen to the south of the western nucleus (SSY99 - Fig. 3, upper right panel; Downes & Solomon 1998 - Fig. 18, upper right panel) would support this interpretation for a non-coplanar component of molecular gas.

Using mean column densities  $N_H = 1.6 \times 10^{20} T_s \text{ cm}^{-2}$  and  $1.3 \times 10^{20} T_s \text{ cm}^{-2}$  for the eastern and western nuclei respectively and semi-major axes  $167 \text{ pc} \times 118 \text{ pc}$  (E) and  $102 \text{ pc} \times 65 \text{ pc}$  (W), corresponding to the radius at which the H I absorption line strength is greater than  $3\sigma$ , we infer H I masses  $M_H = 7.5 \times 10^4 T_s M_\odot$  (E) and  $2.0 \times 10^4 T_s M_\odot$  (W). These masses are  $(1.3-5.1) \times 10^4 T_s^{-1}$  times lower than the mass of molecular gas in the disks derived from the CO observations ( $\sim 10^9 M_\odot$ ; Downes & Solomon 1998, DS98 hereafter; SSY99); given the uncertainty in the CO mass determination, the H I and CO masses would be comparable for high  $T_s \sim 10^4 \text{ K}$ . Assuming the neutral gas is distributed in two circularly rotating disks of radius  $167 \text{ pc}$  (E) and  $102 \text{ pc}$  (W), the observed velocity gradients (see Sect. 3.2) imply dynamical masses  $M_D = 1.1 \times 10^9 (\sin^{-2} i) M_\odot$  (E) and  $1.7 \times 10^8 (\sin^{-2} i) M_\odot$  (W). The H I-inferred dynamical mass for E is slightly lower

than values derived from CO observations (2.4 and  $> 1.9 \times 10^9 (\sin^{-2}i)$   $M_\odot$  for DS98 and SSY99, respectively) and indeed the CO emission (DS98, SSY99) out to a radius of  $\sim 0'.3$  (111 pc), although weak and not fully resolved, appears to show a steeper velocity gradient than that of the HI. For the western nucleus, our dynamical mass is very similar to that inferred by DS98 ( $1.7 \times 10^8 \sin^{-2}i M_\odot$ ) but 10 times lower than that inferred by SSY99 ( $> 1.5 \times 10^9 \sin^{-2}i M_\odot$ ) for a similar disk radius. The reason for this difference is not clear and higher angular resolution CO observations might determine whether the CO is located deeper in the nuclear potential well than the HI.

#### 4.2. Current geometry and history of the merger

The fact that the two nuclei have counterrotating gas disks, indicates that the merger in Arp 220 involved a prograde-retrograde encounter of two gas-rich progenitor disk galaxies. Numerical simulations of such mergers can be found in Mihos & Hernquist (1996, MH96 hereafter). In particular, these simulations show that the prograde and retrograde disks will behave differently during the merger and may also experience different star formation episodes (MH96 - Sect. 4.2). In Arp 220, qualitative comparison between the observations and the models of MH96 suggests that the eastern nucleus, which rotates in the same sense as the 1-kpc CO disk (Scoville et al. 1991; Scoville, Yun & Bryant 1997, SYB97 hereafter; DS98) and 100-kpc HI disk (Hibbard, Vacca & Yun 2000, HVY2000 hereafter) in which it is embedded, represents the retrograde progenitor while the western nucleus and north-western optical plume originate from the prograde progenitor (HVY2000 hereafter).

Initially, during the first close passage, the retrograde disk (and corresponding halo) sweeps up and accretes a significant fraction of the gas of the prograde disk (30% in the prograde-retrograde *planar* encounter simulations of MH96). In Arp 220, the eastern nuclear disk as well as the kiloparsec-scale CO disk (Scoville et al. 1991; SYB97; DS98), which comprise a large fraction of the mass of the system, are probably the result of this process. Thus, given the similarities between the PA and kinematics of these two overlapping disks, it is likely that the two constitute a single (warped) disk, and so we use the term ‘eastern disk’ in the following discussion to refer to the association of these two disks. The second argument in favor of the eastern nucleus being the retrograde one, comes from the morphology of the western nucleus. In the MH96 simulations and after the first close passage, the prograde nucleus has lost up to 50% of its mass, either accreted by the retrograde disk or launched into tidal tails. This is qualitatively consistent with the observed properties of the western disk, which is more compact, less massive than its companion and is likely the origin of the north-western optical plume (HVY2000).

If the western nucleus is indeed the core of the prograde galaxy, this has important implications for the current geometry of the system. Based on the good agreement between the mean velocity of the western disk and the line of sight velocity of gas in the large-scale CO disk at this position (SYB97), previous studies have assumed that the western disk was orbiting in the plane of the ‘large-scale’ CO disk (e.g. see Fig. 7 in SYB97 or Fig. 5 in SSY99). In this context, the deprojected locations of the two nuclei were derived from their mean line of sight velocities, and the western nucleus was placed closer along our line of sight than the eastern nuclear disk (e.g. see Fig. 24 in DS98). However, for the western nucleus to be the prograde nucleus its orbit must pass *behind* the eastern nucleus, so the location of the western nucleus on its orbital path is therefore important. The absence of an  $\text{H}\text{I}$  absorption signature from eastern-disk gas in the spectra of the western nucleus indicates that the western disk lies above the eastern disk, while the mean blueshifted velocity of the western disk with respect to the eastern disk ( $\sim -170 \text{ km s}^{-1}$ , SSY99), permits only the far-sided half of the orbit (see Figure 7); combining these two constraints results in the western disk lying on the orbit quadrant above the eastern disk, on its final inward journey towards collision with the eastern disk (see Figure 7). The presence of disturbed  $\text{H}\text{I}$  in the bridge (B) connecting the two nuclei further supports this merger scenario with the eastern edge of the western disk merging with the main disk.

Continuing our comparison with the models of MH96 and assuming that the eastern nucleus is the retrograde nucleus, we can investigate how and when two important starburst events in Arp 220 fit in such a scenario. The first event is that which gave birth to the galactic superwind and the associated kiloparsec scale bubbles observed in Arp 220 (Heckman, Armus & Miley 1987 1990, HAM90 hereafter; Heckman et al. 1996, HDEW96 hereafter). Given the kinematic expansion time of the bubbles ( $3 \times 10^7 \text{ yr}$ , HDEW96, from HAM90) and the time needed by a (continuous) starburst to deposit significant mechanical energy into its environment ( $< 10^7 \text{ yr}$ , Fig. 56 in Leitherer & Heckman 1995, LH95 hereafter), the starburst powering this outflow must have started a  $10^7$  to  $10^8$  years ago (additional time may have been necessary for the superwind to break out from the gaseous disk). As the orientation of the outflow is roughly perpendicular to the major axis of the eastern disk, it is likely that this starburst took place in this disk. Assuming that the Arp 220 merger is currently in the stage just before the final fusion of the two gas rich systems (i.e.  $t \sim 58\text{-}60$  in Fig. 12 in MH96) this corresponds<sup>7</sup> to  $t \sim 50\text{-}56$  in the simulations. In the simulations, the retrograde disk does indeed experience a continuous period of star formation (which is stronger than

---

<sup>7</sup>The absolute value of the time step in the simulations of MH96 depends on the initial characteristics of the galaxies. For values appropriate for the Milky Way, one time step corresponds to  $t \sim 1.3 \times 10^7 \text{ yr}$  (see MH96 - Sect. 2.1).

in the prograde disk, MH96) during these intermediate times (Fig. 13 in MH96). Note that, assuming that all the mechanical energy deposited by the starburst is injected into the wind, the mechanical luminosity of the superwind ( $\sim 10^{43}$  erg s $^{-1}$ , HDEW96) corresponds to a star formation rate of  $\sim 10\text{--}100$  M $_{\odot}$  yr $^{-1}$  (LH96 - Fig. 56 for a continuous star formation rate). These values are lower than the recent star formation rate estimated in Arp 220 ( $\sim 240$  M $_{\odot}$  yr $^{-1}$ , Anantharamaiah et al. 2000), but are consistent with the models which predict a sharp increase in the star formation rate in the final stage of the merger compared to the intermediate times (MH96 - Fig. 14, second row).

The second starburst event, more recent and probably more violent (consistent with the models of MH96 described above), is the one revealed by the large number of luminous radio supernovae detected in the western nucleus (Smith et al. 1998, SLLD98 hereafter). The rate of type II supernovae inferred from these observations is 1-4 yr $^{-1}$  and corresponds to a star formation rate ranging from 50 to 800 M $_{\odot}$  yr $^{-1}$  (LH95 - Fig. 6 for a continuous star formation rate). This is consistent with the value of 160 M $_{\odot}$  yr $^{-1}$  that can be inferred<sup>8</sup> for the western nucleus from the observations of Anantharamaiah et al. (2000). One striking feature of the distribution is the luminous radio supernovae (SLLD98). Figure 8 shows the positions of the radio supernovae and OH megamaser emission features with respect to the MERLIN 1.4-GHz continuum emission. The fitted positions of the E and W nuclei as derived from the MERLIN 1.4-GHz continuum image (Sect. 3.1) and from similar MERLIN observations made at 5 GHz (Baan, private communication) are also shown. There is a clear offset between the RSN and the nuclear positions, particularly for the western nucleus where the supernovae are located  $\sim 0\rlap{.}^{\prime}1 - 0\rlap{.}^{\prime}15$  south of the western nucleus and consequently, the compact central feature of the W1 OH megamaser emission (Lonsdale et al. 1998a 1998b) coincides with the position of the western nucleus. In a simplistic model of star formation occurring in an edge on disk, the RSN distribution would be expected to coincide with the nucleus. However, if star formation is occurring throughout the disk and the nearside of the disk is tilted slightly to the south, as suggested by NICMOS observations of Arp 220 (Scoville et al. 1998), RSN in the near half of the disk would be more easily visible. In particular a moderate column density of ionized gas associated with the bulge-like component suggested by Scoville et al. (1998) and the longer path length to RSN on the far side of the disk would result in RSN radio emission being free-free absorbed. Emission measures  $1.1 \times 10^7 \lesssim \text{EM} \lesssim 2.4 \times 10^7$  cm $^{-6}$  pc, corresponding to optical depths  $1.2 \lesssim \tau \lesssim 2.6$ , would be required to free-free absorb emission from RSN with the same flux density at 1.67 GHz as those observed by SLLD98, assuming a uniform screen of ionized

---

<sup>8</sup>Roughly two thirds of the H92 $\alpha$  line emission in their observations come from the western nucleus. If we scale the total star formation rate (240 M $_{\odot}$  yr $^{-1}$ ) accordingly, this gives a star formation rate for the western nucleus alone of  $\sim 160$  M $_{\odot}$  yr $^{-1}$ .

absorbing gas with an electron temperature  $T_e=10^4$  K. Such emission measures compare well with those inferred from radio recombination line observations (Anantharamaiah et al. 2000) which, however, suggest more complex models for the ionized gas than a single density uniform slab. Alternatively, the RSN positional offset might be a consequence of positional uncertainty of the MERLIN observations (see Sect. 2.1.1); future observations are required to confirm the registration of MERLIN and VLBA images.

## 5. Conclusions

We have presented the highest angular resolution observations to date of the neutral gas distribution and kinematics and the  $\lambda 21$ -cm continuum emission in the central  $\sim 900$  pc of the advanced merger system, Arp 220. Spatially resolved H I absorption was detected against the morphologically complex and extended  $\lambda 21$ -cm radio continuum emission; the two nuclei are spatially well separated at this resolution and a velocity gradient is clearly visible across each nucleus consistent with the H I being in two counterrotating disks of neutral hydrogen, with a small bridge of gas connecting the two. The column densities across the two nuclei are high, lying in the range  $8 \times 10^{19} T_s(K) \lesssim N_H \lesssim 2.4 \times 10^{20} T_s(K) \text{ cm}^{-2}$  ( $T_s$  is spin temperature) and corresponding to optical extinctions of  $0.052 T_s(K) \lesssim A_V \lesssim 0.155 T_s(K)$  mag, with the higher column densities being found in the eastern nucleus. Velocity gradients of  $1010 \pm 20 \text{ km s}^{-1} \text{ kpc}^{-1}$  in PA  $\sim 55^\circ$  and  $830 \pm 20 \text{ km s}^{-1} \text{ kpc}^{-1}$  in PA  $\sim 270^\circ$  across the eastern and western nuclei respectively imply corresponding dynamical masses  $M_D = 1.1 \times 10^9 (\sin^{-2} i) M_\odot$  (E) and  $1.7 \times 10^8 (\sin^{-2} i) M_\odot$  (W), assuming the neutral gas is distributed in two thin, circularly rotating disks.

We propose a new merger geometry in which the two nuclei are in the final stages of merging, similar to conclusions drawn from CO studies (SSY99), but instead of being coplanar with the main CO disk (in which the eastern nucleus is embedded), we suggest that the western nucleus lies above it and will soon complete its final merger with the main disk. The bridge of H I seen connecting the two nuclei further supports this scenario. We suggest that the collection of radio supernovae (RSN), detected in VLBA studies, in the more compact western nucleus represent the second burst of star formation associated with this final merger stage and that free-free absorption due to ionised gas in the bulge-like component can account for the observed RSN distribution.

## 6. Acknowledgements

We thank Toby Moore, Nick Scoville, John Porter, Andrew Wilson, Sylvain Veilleux and Lee Mundy for useful discussions and Peter Thomasson for help with the MERLIN data. We are grateful to Willem Baan for kindly providing MERLIN 5-GHz-derived positions prior to publication and the anonymous referee for useful comments. CGM acknowledges financial support from The Royal Society. This research was partially supported by NSF grant AST9527289 to the University of Maryland. MERLIN is a U.K. national facility operated by the University of Manchester on behalf of the Particle Physics and Astronomy Research Council. This research has made use of NASA’s Astrophysics Data System Abstract Service (ADS) and the NASA/IPAC Extragalactic Database (NED), which is operated by the Jet Propulsion Laboratory, California Institute of Technology, under contract with the National Aeronautics and Space Administration.

## REFERENCES

Anantharamaiah, K.R., Viallefond, F., Mohan, N.R., Goss, W.M., Zhao, J.H. 2000, *ApJ*, 537, 613

Baan, W.A. & Haschick, A.D. 1984, *ApJ*, 279, 541

Baan, W.A., Güsten, R., Haschick, A.D. 1986, *ApJ*, 305, 830

Baan, W.A., van Gorkom, J., Schmeltz, J.T. & Mirabel, F.I. 1987, *ApJ*, 313, 102

Baan, W.A. & Haschick, A.D. 1995, *ApJ*, 454, 745

Baars, J.W.M., Genzel, R., Pauliny-Toth, I.I.K. & Witzel, A., 1977, *A&A*, 61, 99

Barnes, J.E. & Hernquist, L.E. 1991, *ApJ*, 370, L65

Browne, I.W.A., Wilkinson, P.N., Patnaik, A.R. & Wrobel, J.M. 1998, *MNRAS*, 293, 257

Carilli, C.L. & Taylor, G.B. 2000, *ApJ*, 532, L95

Clements, D.L., Sutherland, W.J., Saunders, W., McMahon, R.G. 1996a, *MNRAS*, 279, 477

Clements, D.L., Sutherland, W.J., Saunders, W., McMahon, R.G., Maddox, S., Efstathiou, G.P., Rowan-Robinson, M., Lawrence, A., 1996b, *MNRAS*, 279, 459

Clements, D.L. & Baker, A.C. 1996, *A&A*, 314, L5

Cole, G.H.J., Mundell, C.G. & Pedlar, A. 1998, MNRAS, 300, 656

Condon, J.J. & Dressel, L.L. 1978, ApJ, 221, 456

Condon, J.J., Helou, G. Sanders, D.B., Soifer, B.T. 1990, ApJS, 73, 359,

Dermer, C.D., Bland-Hawthorn, J., Chiang, J. & McNaron-Brown, K. 1997, ApJ, 484, L121

Downes, D. & Solomon, P.M. 1998, ApJ, 507, 615

Frerking, M.A., Langer, W.D. & Wilson, R.W. 1982, ApJ, 262, 590

Genzel, R., et al. 1998, ApJ, 498, 579

Greisen E.W. & Murphy, P.P. 1998, in The AIPS Cookbook, chapter 9, online at  
[<http://www.cv.nrao.edu/aips/cook.html>]

Heckman, T.M., Armus, L. & Miley, G.K. 1987, AJ, 92, 276

Heckman, T.M., Armus, L. & Miley, G.K. 1990, ApJS, 74, 833

Heckman, T.M., Dahlem, M., Eales, S.A., Fabbiano, G., Weaver, K. 1996, ApJ, 457, 616

Heiles, C. & Kulkarni, S. 1988, in Galactic and Extragalactic Radio Astronomy, ed. K. Kellerman & G. Verschuur (2nd ed.; Berlin: Kluwer), 95

Hibbard, J.E., Vacca, W.D. & Yun, M.S., AJ, 2000, 119, 1130

Lacy, J.H., Knacke, R., T.R. Geballe & Tokunaga, A.T. 1994, ApJ, 428, L69

Lonsdale, C.J., Diamond, P.J., Smith, H.E., Lonsdale, C.J. 1998, ApJ, 493, L13

Erratum, Lonsdale et al. 1998b, ApJ, 494, L239

Lutz, D., Veilleux, S. & Genzel, R. 1999, ApJ, 517, L13

Mihos, J.C. & Hernquist, L. 1994, ApJ, 431, L9

Mihos, J.C. & Hernquist, L. 1996, ApJ, 464, 641

Mundell, C.G., Pedlar, A., Baum, S.A., O'Dea, C.P., Gallimore, J.F. & Brinks, E. 1995, MNRAS, 272, 355

Mirabel, I.F. & Sanders, D.B. 1988, ApJ, 335, 104

Norman, C.A. & Scoville, N. 1988, ApJ, 322, 124

Norris, R.P. 1988, MNRAS, 230, 345

Patnaik, A.R., Browne, I.W.A., Wilkinson, P.N. & Wrobel, J.M. 1992, MNRAS, 254, 655

Peck, A.B. & Taylor, G.B. 1998, ApJ, 502, L23

Rieke, G. H., 1988, ApJ, 331, L5

Rousset A. 1992, Contribution des méthodes numériques au dépouillement des données du spectrographe intégral de champ TIGER, PhD Thesis, Univ. J.Monnet de Saint-Etienne

Sakamoto, K., Scoville, N.Z., Yun, M.S., Crosas, M., Genzel, R., Tacconi, L.J. 1999, ApJ, 514, 68

Sanders, D.B., Soifer, B.T., Helias, J.H., Neugebauer, G., Matthews, K. 1988, ApJ, 328, L35

Sanders, D.B., Scoville, N.Z. & Soifer, B.T. 1991, ApJ, 370, 158

Sanders, D.B. & Mirabel, I.F. 1996, ARA&A, 34, 749

Scoville, N.Z., Yun, M.S. & Bryant, P.M. 1997, ApJ, 484, 702,

Scoville, N.Z. et al. 1998, ApJ, 492, L107

Smith, H.E., Lonsdale, C.J., Lonsdale, C.J., Diamond, P.J. 1998, ApJ, 493, L17

Soifer, B.T., Sanders, D.B., Neugebauer, G., Danielson, G.E., Lonsdale, C.J., Madore, B.F., Persson, S.E. 1986, ApJ, 303, L41

Soifer, B.T., Houck, J.R. & Neugebauer, G. 1987, ARAA, 25, 187

Staveley-Smith, L. & Davies, R.D., 1987, MNRAS, 224, 953

van Moorsel, G., Kemball, A., & Greisen, E. 1996, in Astronomical Data Analysis Software and Systems V, ASP Conf. Series 101, eds., Jacoby, G.H. & Barnes, J., 37

Veilleux, S., Sanders, D.B. & Kim, D.-C. 1999, ApJ, 522, 139

White R.L. & Becker, R.H. 1992, ApJS, 79, 331

Wilkinson, P.N., Browne, I.W.A., Patnaik, A.R., Wrobel, J.M. & Sorathia, B. 1998, MNRAS, 300, 790

Fig. 1.— MERLIN 1.4-GHz radio continuum image of the central  $\sim 900$  pc of Arp 220. The beam size, indicated by a circle on the lower left corner, is  $0''.22$ . The two nuclei are labelled E (east) and W (west), with the labels (A, B, C) assigned by BH95 given in parentheses. The weak, extended spur of emission, to the north-west of W, is labelled T. The contour levels, in multiples of  $3 \times \text{rms}$ , are  $(-1, 1, 2, 4, 8, 16, 32, 64, 128) \times 0.33 \text{ mJy beam}^{-1}$ .

Fig. 2.— Channel maps of H I absorption in Arp 220. The 1.4-GHz radio continuum image is shown the the top left panel with the beamsize, shown as a circle, in the lower left corner of this image. The individual channel maps, in which H I absorption is detected, are labelled according to the central velocity of each channel - indicated in the top right corner of each line image; the (dotted) contour levels in the absorption channel maps are  $(-64, -32, -16, -8, -4, -2, -1, 1) \times 1.5 \text{ mJy beam}^{-1}$ .

Fig. 3.— **Central image** : 1.4-GHz radio continuum map with the contours of the H I absorption velocity field superimposed (contours from  $5300$  to  $5600 \text{ km s}^{-1}$ , in steps of  $50 \text{ km s}^{-1}$ ). **Profiles** : 1.4-GHz radio continuum and H I absorption line velocity profiles at eight selected locations. Properties of the radio continuum and H I absorption at these locations are given in Tab. 1.

Fig. 4.— **Left panel** : 1.4-GHz radio continuum map with the contours of the H I absorption velocity field superimposed (contours from  $5300$  to  $5600 \text{ km s}^{-1}$ , in steps of  $50 \text{ km s}^{-1}$ ). **Middle panel** : Map of the equivalent hydrogen column density for the main H I absorption component (assuming a spin temperature of  $100 \text{ K}$ ), as derived by multiple Gaussian fitting of the H I absorption line (see Sect. 2.2). Only regions where the 1.4-GHz continuum emission and the depth of the absorption line were stronger than  $1.5 \text{ mJy beam}^{-1}$  have been mapped (i.e. 3 times the typical rms of the noise in the spectra). The contours are those of the velocity field of the main H I absorption component (contours from  $5300$  to  $5600 \text{ km s}^{-1}$ , in steps of  $50 \text{ km s}^{-1}$ ), derived from the same fit. **Right panel** : Velocity field of the main H I absorption component, as derived by multiple Gaussian fitting of the H I absorption line (see Sect. 2.2). Again, we have only mapped regions where the 1.4-GHz continuum emission and the depth of the absorption line were stronger than  $1.5 \text{ mJy beam}^{-1}$  (i.e. 3 times the typical rms of the noise in the spectra). The contours are those of the 1.4-GHz radio continuum map (dotted contours :  $2, 4, 6$  and  $8 \text{ mJy beam}^{-1}$ ; solid contours :  $10, 20, 30, 40, 50$  and  $60 \text{ mJy beam}^{-1}$ ). North is up and east is left throughout.

Fig. 5.— Velocity profiles of the H I absorption line at three selected locations of the eastern nucleus (see Fig. 3 and Tab. 1), with the fitted profiles superimposed (single component Gaussian fit : dashed line; two component Gaussian fit : dotted line, central panel only). The upper part of each panel displays the residuals of the subtraction of the fitted spectrum

to the observed one (single component Gaussian fit : solid line; two component Gaussian fit : dotted line, central panel only).

Fig. 6.— 1.4-GHz radio continuum and velocity profiles of the H I absorption line at three selected locations of the western nucleus (see Fig. 3 and Table 1), with the fitted profiles superimposed (single component Gaussian fit : dashed line; multiple component Gaussian fit : dotted line). The upper part of each panel displays the residuals of the subtraction of the fitted spectrum to the observed one (single component Gaussian fit : solid line; multiple component Gaussian fit : dotted line).

Fig. 7.— Sketch of merging geometry of prograde western disk with (retrograde) eastern/main disk, as viewed on the sky. Small arrows indicate rotation direction of each disk; the orbital/merger path of the western disk is also indicated.

Fig. 8.— 1.4-GHz MERLIN radio continuum of Arp 220 with the locations of radio supernovae (RSN) and OH masers (from SLLD98) indicated. The position of the E and W nuclei as derived from MERLIN radio continuum observations at 1.4 GHz (present paper) and 5 GHz (Baan, private communication) are also shown.

Figure 1

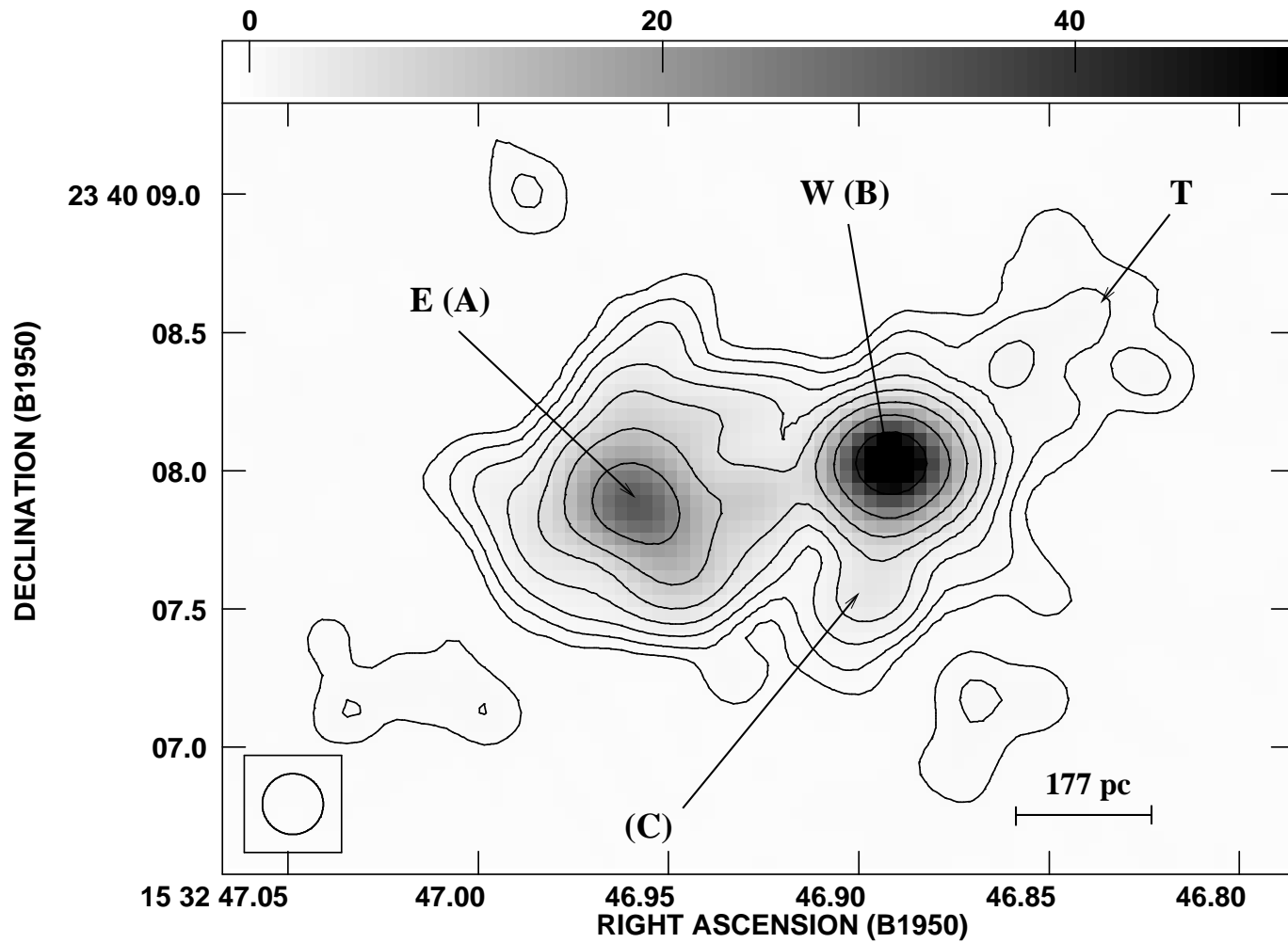
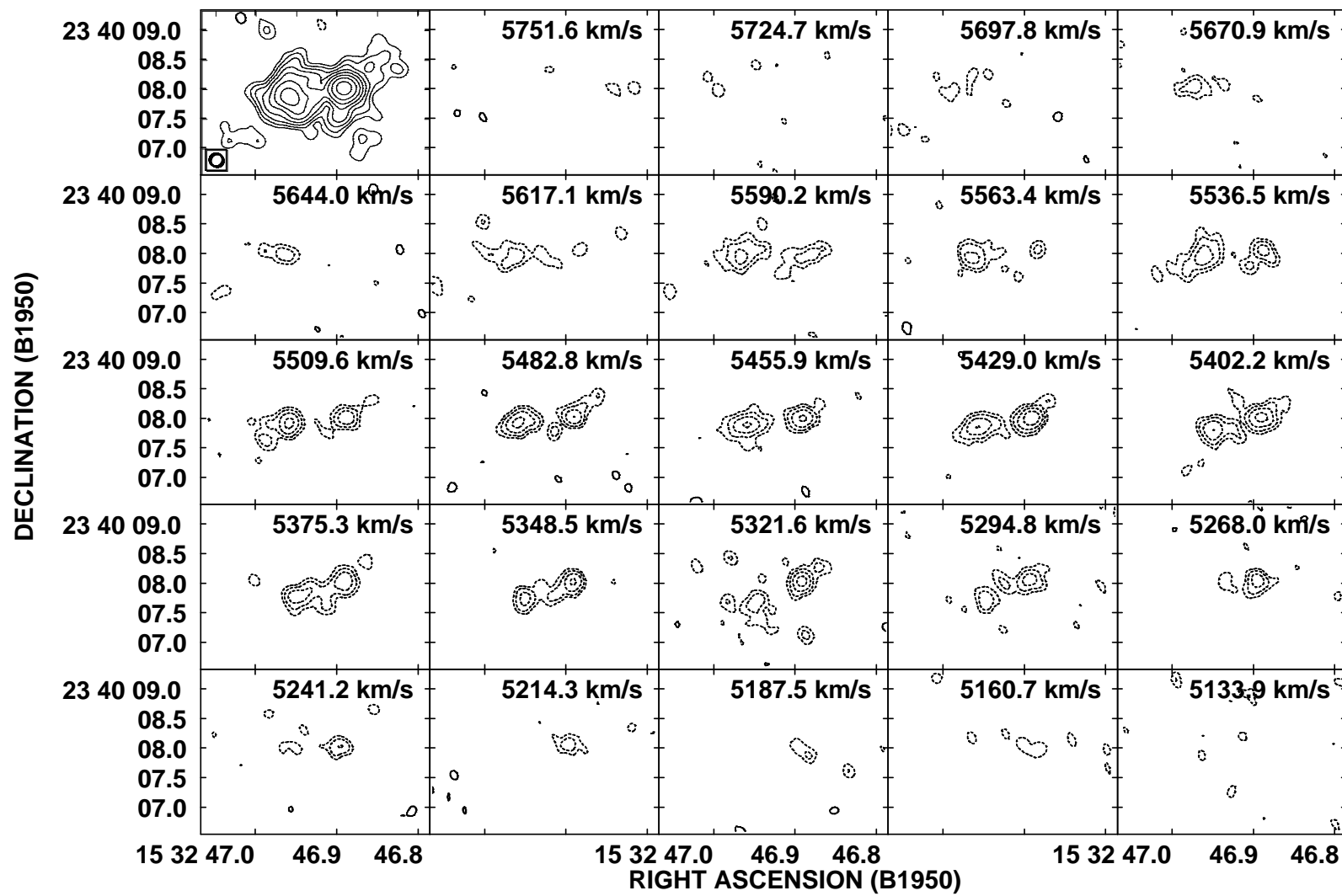


Figure 2



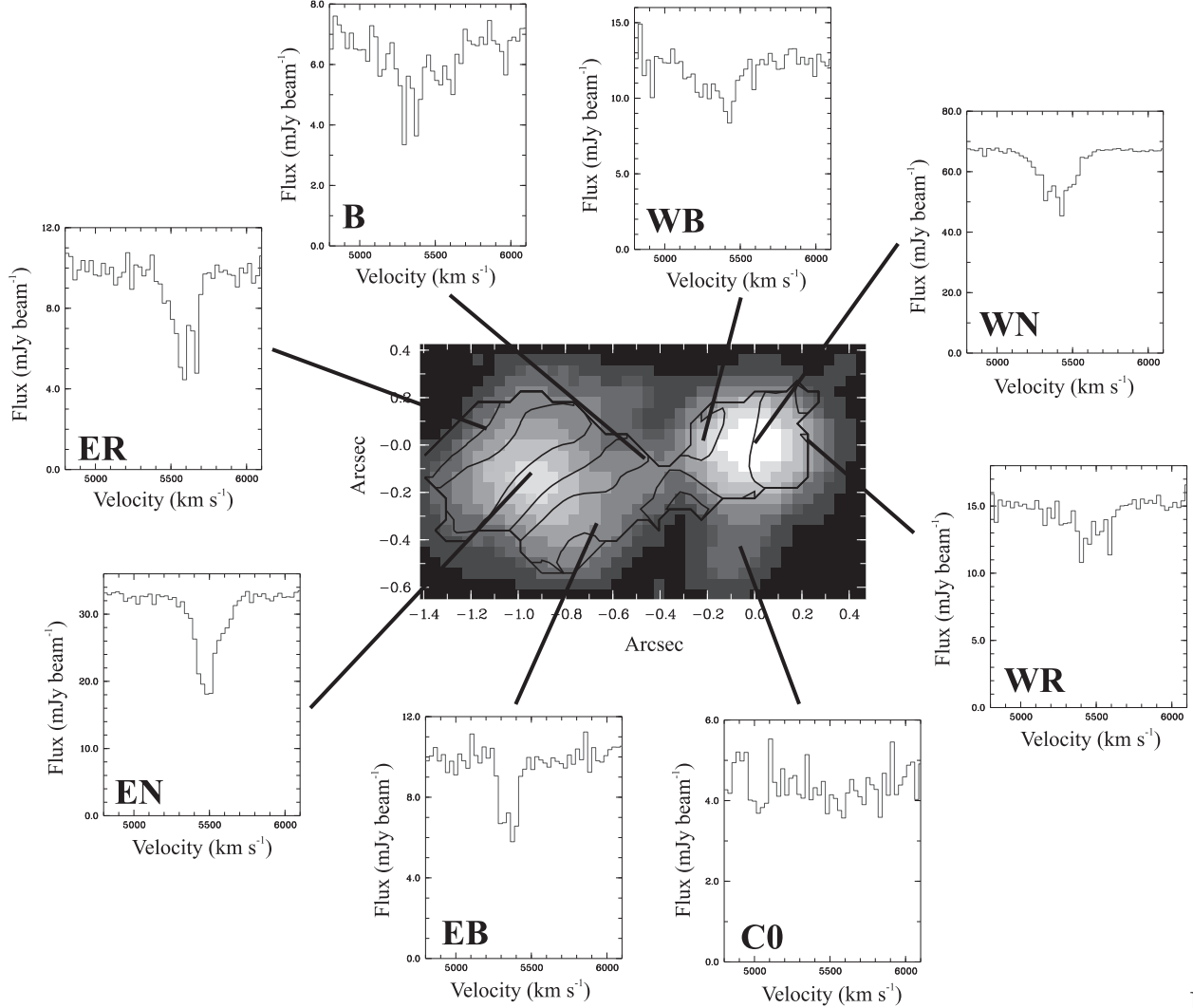


Figure 3

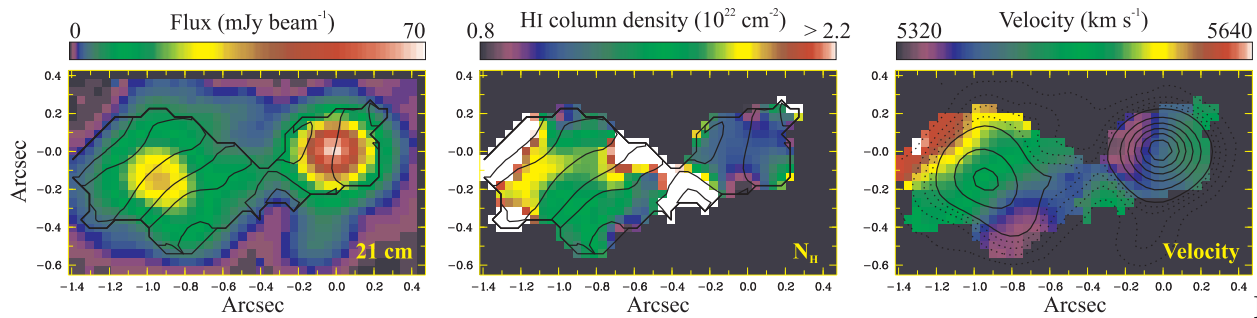


Figure 4

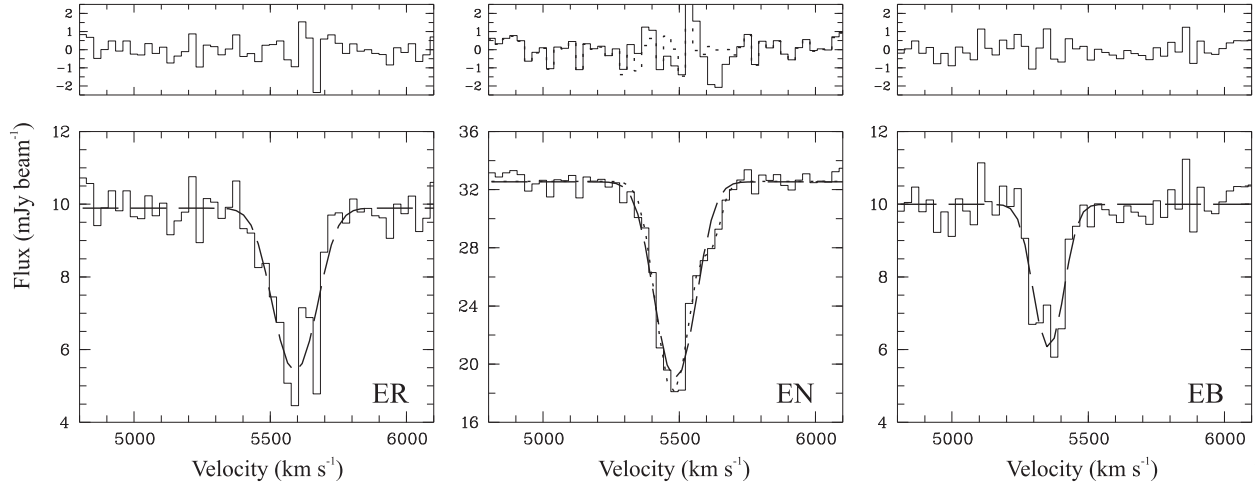


Figure 5

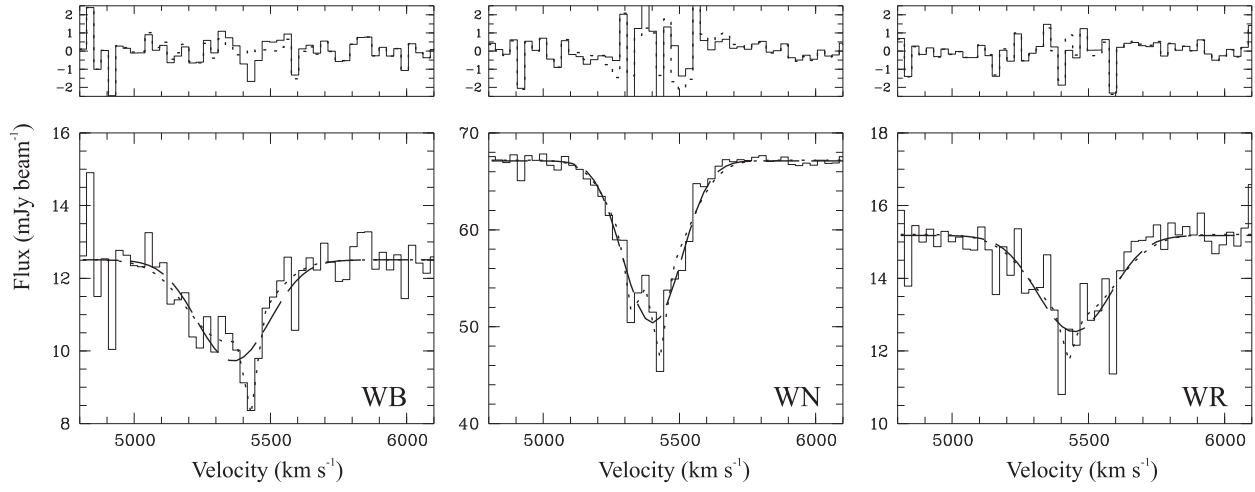


Figure 6

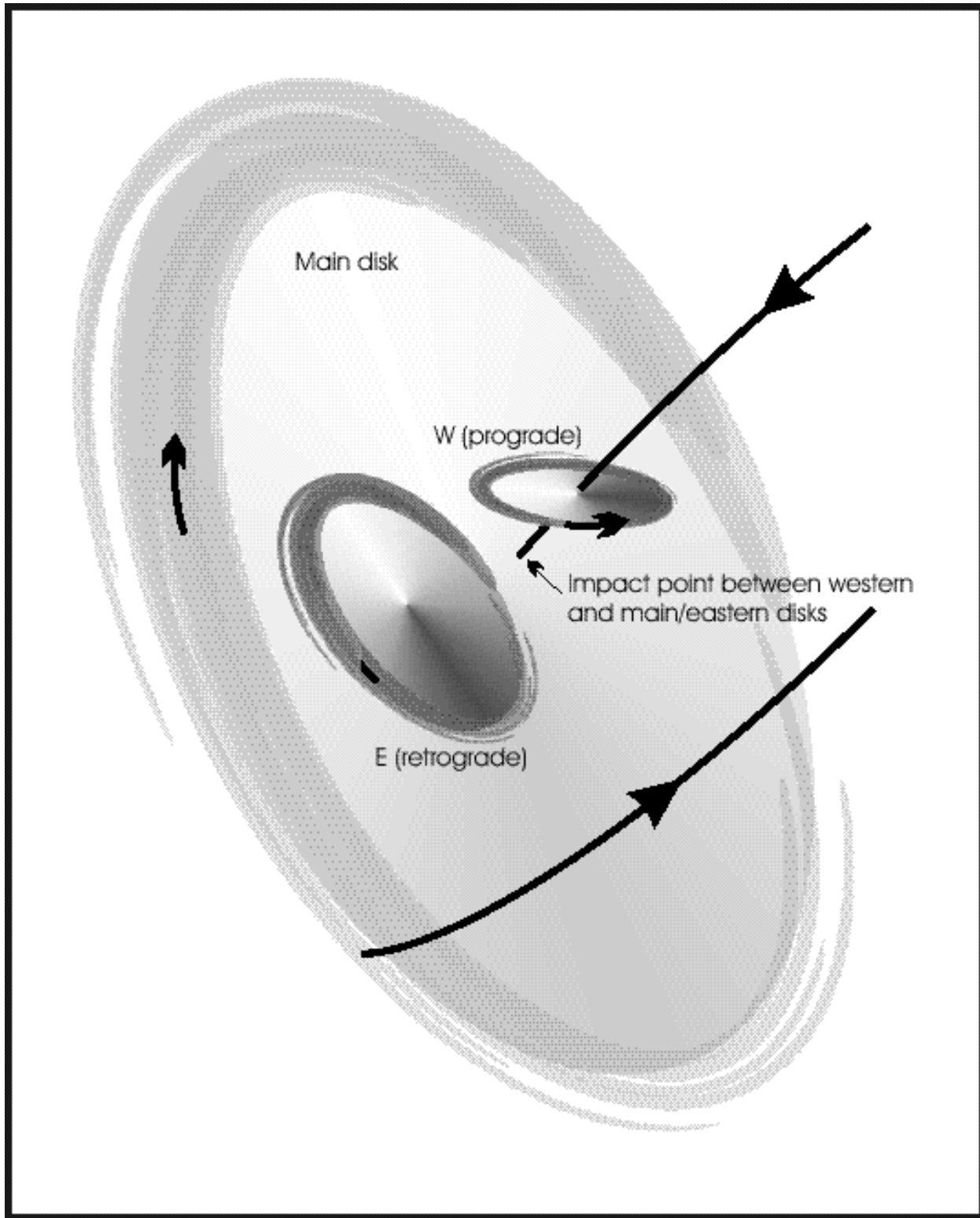


Figure 7

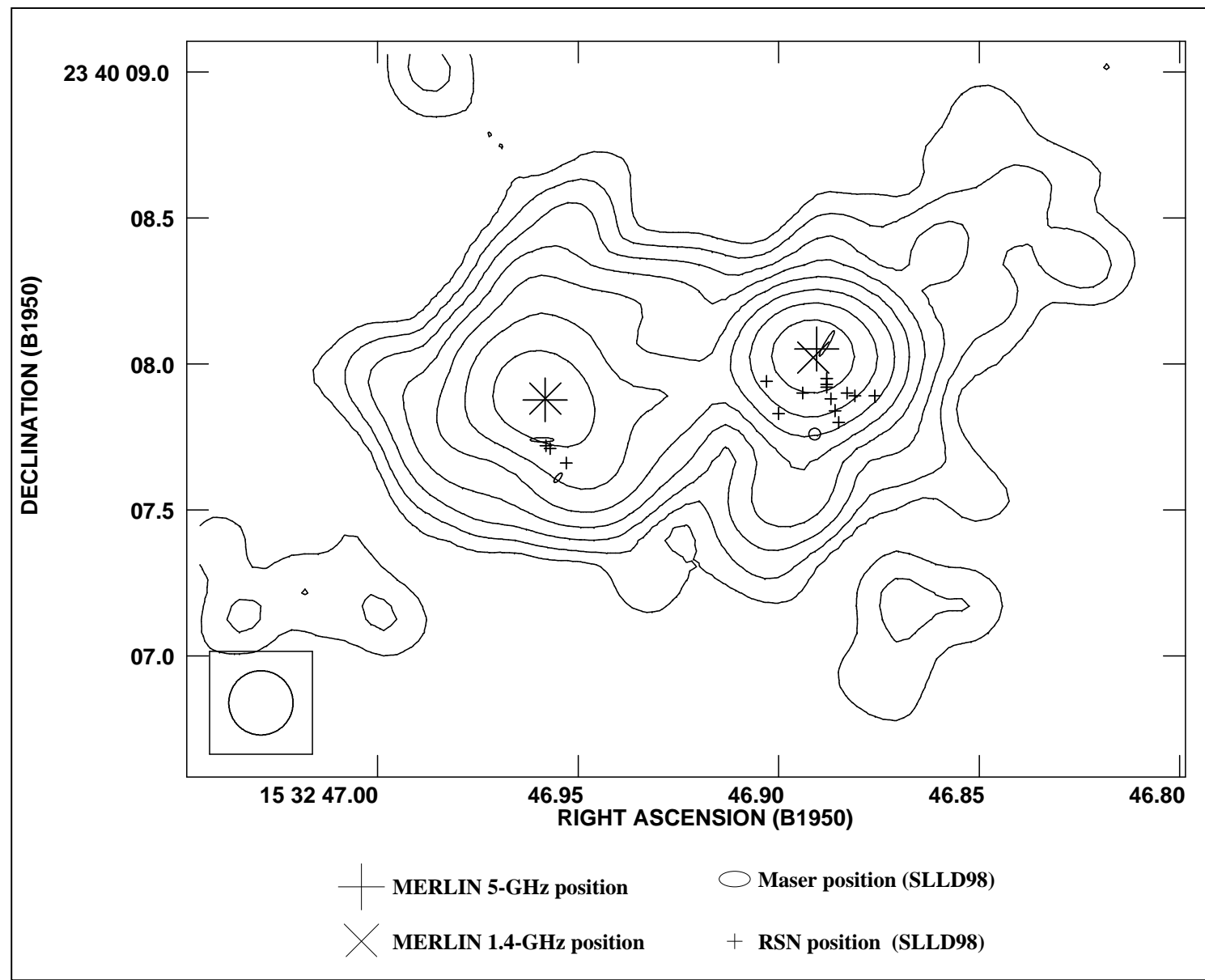


Figure 8

Table 1: Results of single and multiple component Gaussian fitting of spectra at seven selected locations where H I absorption is detected (see Fig. 3). The offset ( $\Delta\alpha, \Delta\delta$ ) of each location is given relative to WN, where the derived position for WN is  $\alpha_{1950} = 15^h32^m46\rlap{.}^s89142s$ ,  $\delta_{1950} = 23^\circ40'08\rlap{.}''0215$ . For each spectral component the measured 1.4-GHz continuum flux density ( $F_{1.4\text{GHz}}$ ) is given along with derived H I column density ( $N_{\text{H}}/T_{\text{S}}$ ) and corresponding visual extinction ( $A_{\text{V}}/T_{\text{S}}$ ) for a spin temperature of  $T_{\text{S}}$ , absorption line velocity centroid and full width at half maximum (FWHM). Details on the Gaussian fitting procedure can be found in Sect. 2.2.

	B	ER	EN	EB	WB	WN	WR
$\Delta\alpha$ (arcsec)	−0.405	−1.125	−0.945	−0.675	−0.270	0	+0.225
$\Delta\delta$ (arcsec)	−0.090	+0.045	−0.135	−0.360	0	0	0
<b>Single component Gaussian fitting</b>							
$F_{1.4\text{GHz}}$ (mJy beam $^{-1}$ )	6.86±0.39	9.89±0.52	32.53±1.63	10.00±0.52	12.51±0.63	67.12±3.36	15.18±0.77
$N_{\text{H}}/T_{\text{S}}$ ( $10^{20}$ cm $^{-2}$ )	2.4±0.4	1.99±0.15	1.68±0.04	1.17±0.11	1.46±0.16	1.32±0.02	1.13±0.15
$A_{\text{V}}/T_{\text{S}}$ ( $10^{-2}$ mag)	15.5±2.6	12.9±1.0	10.9±0.3	7.6±0.7	9.4±1.0	8.5±0.1	7.3±1.0
Velocity (km s $^{-1}$ )	5387±20	5591±5	5486±19	5354±5	5364±13	5401±2	5448±12
FWHM (km s $^{-1}$ )	390±70	169±12	161±5	120±12	300±40	238±5	300±40
<b>Multiple component Gaussian fitting</b>							
$F_{1.4\text{GHz}}$ (mJy beam $^{-1}$ )	–	–	32.57±0.1.63	–	12.51±0.64	67.19±3.36	15.20±0.78
▷ Main component properties							
$N_{\text{H}}/T_{\text{S}}$ ( $10^{20}$ cm $^{-2}$ )	–	–	1.52±0.05	–	1.22±0.18	1.10±0.03	1.08±0.15
$A_{\text{V}}/T_{\text{S}}$ ( $10^{-2}$ mag)	–	–	9.8±0.3	–	7.9±1.2	7.1±0.2	7.0±1.0
Velocity (km s $^{-1}$ )	–	–	5478±2	–	5336±18	5404±3	5449±16
FWHM (km s $^{-1}$ )	–	–	132±5	–	317±50	270±7	340±50
▷ Sub-component properties							
$N_{\text{H}}/T_{\text{S}}$ ( $10^{20}$ cm $^{-2}$ )	–	–	0.20±0.03	–	< 0.1	0.10±0.01	< 0.08
$A_{\text{V}}/T_{\text{S}}$ ( $10^{-2}$ mag)	–	–	1.3±0.2	–	–	0.6±0.1	–
Velocity (km s $^{-1}$ )	–	–	5618±6	–	5326 <sup>a</sup>	5326 <sup>a</sup>	5326 <sup>a</sup>
FWHM (km s $^{-1}$ )	–	–	80±12	–	50 <sup>a</sup>	50 <sup>a</sup>	50 <sup>a</sup>
$N_{\text{H}}/T_{\text{S}}$ ( $10^{20}$ cm $^{-2}$ )	–	–	–	–	0.26±0.05	0.15±0.02	0.10±0.04
$A_{\text{V}}/T_{\text{S}}$ ( $10^{-2}$ mag)	–	–	–	–	1.7±0.3	1.0±0.1	0.6±0.3
Velocity (km s $^{-1}$ )	–	–	–	–	5428 <sup>a</sup>	5428 <sup>a</sup>	5428 <sup>a</sup>
FWHM (km s $^{-1}$ )	–	–	–	–	50 <sup>a</sup>	50 <sup>a</sup>	50 <sup>a</sup>

<sup>a</sup> Parameter set to a fixed value during the fit.